CHEMISTRY OF MATERIALS

pubs.acs.org/cm Article

Structural Investigation of Silver Vanadium Phosphorus Oxide ($Ag_2VO_2PO_4$) and Its Reduction Products

He Sun, Blake A. Hammann, Alexander B. Brady, Gurpreet Singh, Lisa M. Housel, Esther S. Takeuchi, Kenneth J. Takeuchi, Amy C. Marschilok,* Sophia E. Hayes,* and Lisa F. Szczepura*

Cite This: *Chem. Mater.* 2021, 33, 4425−4434 Read Online

ACCESS | Metrics & More | Article Recommendations | Supporting Information

ABSTRACT: A combination of powder XRD, solid-state NMR, and electrochemical impedance spectroscopy (EIS) is utilized to study the high capacity primary lithium battery cathode material ($Ag_2VO_2PO_4$), as well as its electrochemically reduced counterparts. EIS provides information about the reduction process, and powder XRD is useful in determining the structure of pristine SVPO and the 1 electron equivalent (1ee) reduced materials, which are crystalline and contain edge-sharing VO_6 units. However, SVPO becomes increasingly paramagnetic and amorphous as reduction proceeds from 1ee up to 3ee. Here we probe the VO_6 coordination environment in the parent SVPO material as well as the reduced materials using both static and magic-angle spinning solid-state ^{51}V NMR spectroscopy. The chemical shielding anisotropy (CSA) and electric field gradient (EFG) NMR tensors were determined through fitting of the spinning side bands or via density functional theory (CASTEP), or both. These tensors provide useful insight into the structure of the reduced materials. All materials exhibit similar isotropic chemical shifts for ^{51}V; however, other line-shape elements vary as the coordination environment changes upon reduction. We find that the ^{51}V NMR tensor parameters (δ_{CS} and C_Q) are better at indicating changes to the local environment than the isotropic chemical shift.

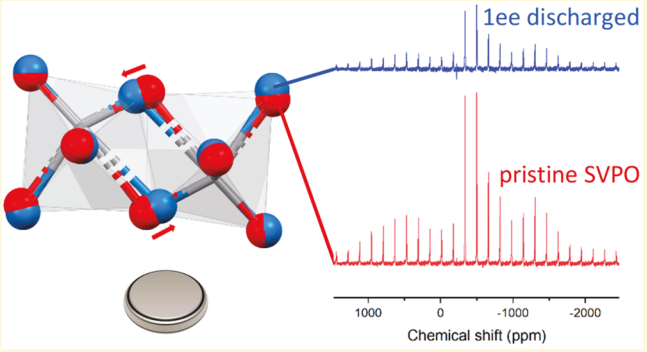

INTRODUCTION

Silver vanadium oxide ($Ag_2V_4O_{11}$ or SVO) and $LiFePO_4$ are two commercially significant cathode materials in lithium-based batteries. SVO has been used for over 25 years as a cathode material in primary batteries most commonly found in implantable cardiac defibrillators (ICDs).[1,2] Vanadium has the potential to undergo multiple electron transfers leading to the generation of high charge density materials; this is a key advantage of SVO and other vanadium-based battery materials. $LiFePO_4$ is one of the best-known phosphate-containing cathode materials for secondary lithium ion batteries on the market.[3,4] While most phosphate materials show enhanced thermal and chemical stability compared with other cathode materials, they often display inherently low conductivity which limits electrochemical performance.[5−9] On the basis of the success of SVO and $LiFePO_4$, there has been interest in examining the properties of silver vanadium phosphorus oxide, $Ag_2VO_2PO_4$ (SVPO), a vanadium phosphate material first prepared in 1993.[10] This material is known to be a high charge density material. However, like $LiFePO_4$, SVPO also has an inherently low conductivity. In the case of $LiFePO_4$, attempts to improve conductivity in commercial batteries include minimizing particle size, coating particles with a conductive material, or doping the material to enhance conductivity.[11−14] Of interest is that SVO and copper vanadium oxides (e.g., $Cu_{1.1}V_4O_{11}$) form metal nanoparticles (Ag^0 and Cu^0, respectively) and nanowires (or dendrites) upon reduction, leading to an increase in the conductivity of these materials as discharge proceeds.[15−18] In 2009, Takeuchi and co-workers found that reduction of lithium-based electrochemical cells utilizing $Ag_2VO_2PO_4$ (SVPO) as the cathode material led to silver metal deposition, resulting in a significant increase (i.e., 15 000 fold) in the conductivity of the material.[19] The ability to generate a conductive matrix in situ in this vanadium phosphate material has led to an increased interest in SVPO as a next generation electrochemical storage material.

In 2007, Greenbaum and co-workers analyzed silver vanadium oxide (SVO) using spectroscopic techniques (solid-state NMR and XAS). In their report, pristine and reduced samples of the commercially important SVO were analyzed by ^{7}Li and ^{51}V SSNMR and silver XAS.[20] These

Received: February 7, 2021
Revised: May 24, 2021
Published: June 9, 2021

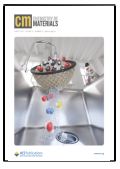

techniques revealed structural details which could not otherwise be determined using X-ray diffraction techniques. As mentioned above, the related silver vanadium phosphorus oxide SVPO ($Ag_2VO_2PO_4$) has attracted attention because of its high capacity and the enhanced stability inherent in phosphate-based materials. However, the amorphization of SVPO that takes place during discharge[21] means that diffraction techniques become less suited for elucidating local structural changes as reduction proceeds. A grand challenge in materials chemistry is characterizing solids, such as electrode materials, where there is a lack of long-range order. Here we examine the bimetallic phosphate material SVPO, using solid-state NMR spectroscopy (focusing on ^{51}V SSNMR), EIS, and powder XRD to gain insight into the local structure of this battery cathode material.

The ^{51}V isotope has a high natural abundance of ^{51}V (99.76%), making it an attractive nucleus for NMR spectroscopy. Even though it is quadrupolar (I = 7/2 for ^{51}V), the low quadrupolar moment (0.05 barn) and high receptivity make it more amenable to study.[22] The solid-state NMR spectroscopy (SSNMR) of vanadium-containing systems has proven valuable in exploring inorganic vanadium oxide catalysts, vanadium containing proteins, and both vanadyl and vanadate species, which are of interest in the treatment of diabetes.[23−27] On the basis of experimental solid-state NMR spectra and the XRD-proposed structure, the local environment can be further refined or confirmed with the help of ab initio methods such as density functional theory (DFT). Thus, key structural information that can be obtained from ^{51}V SSNMR plus DFT calculations includes information such as number and types of coordinated atoms and structural information such as symmetry and association of vanadium−oxygen polyhedra.[22] Here we present the ^{51}V SSNMR spectroscopy of SVPO, $Ag_2VO_2PO_4$ as well as several electrochemically discharged SVPO samples from 1 to 3 electron equivalents. The discharged samples were also analyzed by XRD to obtain structural information. Computation of NMR tensors for three different structural models (two of which were previously published) were performed with the DFT package Cambridge Sequential Total Energy Package (CASTEP). Experimental NMR data and computed NMR parameters were compared. Structural changes of SVPO manifested by the vanadium local environment along the discharge process could be monitored with solid-state NMR, DFT, and powder XRD, when possible. Solid-state NMR and DFT, along with EIS and powder XRD, enabled us to monitor the vanadium local environment along the discharge process, providing insight into the impact of discharge on the SVPO structure.

EXPERIMENTAL SECTION

Synthesis and Characterization. A hydrothermal method adapted from Kang et al. was used to prepare silver vanadium phosphate ($Ag_2VO_2PO_4$).[10] The vessel for the aqueous reaction was a 23 mL Teflon-lined stainless steel autoclave (Parr). Silver oxide (Ag_2O, Alfa AESAR), vanadium(V) oxide (V_2O_5, Alfa AESAR), and phosphoric acid (H_3PO_4) (molar ratio Ag:V:P = 2:1:6, typical scale of product 500 mg) were mixed in 11 mL of water and heated at 230 °C for 96 h. A yellow solid was collected via vacuum filtration. Differential scanning calorimetry (DSC) was conducted up to 580 °C at 5 °C/min to test for sample purity. A Rigaku SmartLab powder diffractometer with a DTex detect and 5° Soller-slits was used to collect an X-ray diffraction (XRD) pattern from 5° to 90° 2θ. The XRD pattern was used to determine crystal structure and was indexed to PDF no. 01-081-2149.

Discharge Experiments. Coin cells were assembled using a Li metal anode and $Ag_2VO_2PO_4$ cathode (LillAg$_2$VO$_2$PO$_4$) with 1 M lithium hexafluorophosphate ($LiPF_6$) electrolyte in 30:70 ethylene carbonate/dimethyl carbonate. Discharge was performed at a rate of C/300 to 1ee, 2ee, and 3ee limits with a Maccor 4000 series battery tester at 30 °C using a postassembly open circuit potential of about 3.40−3.55 V. The cathode material was recovered postdischarge by dismantling the cells inside an inert atmosphere glovebox, pulverizing the cathode pellets, and rinsing the cathode material with pure dimethyl carbonate.

Powder Diffraction. Synchrotron powder X-ray diffraction (XRD) was performed at the 28-ID beamline at NSLS-II. The powder sample was packed into a Kapton tube, and the sample distance was calibrated using an LaB_6 powder sample. The beam wavelength was calibrated to 0.2388 Å. Diffraction data were detected using a 16-in. CsI-scintillator fitted to an amorphous silicon flat panel. The two-dimensional data were integrated using GSAS-II.[28] The diffraction data were analyzed by Rietveld method, using GSAS-II.[28] Raw and refined data are provided (Supporting Information Figure S1). Instrumental broadening was calculated using an LaB_6 powder sample. A 10-term polynomial background was used. Lattice parameters, atomic positions, and Debye−Waller factors were refined. Crystallite size and microstrain broadening were found to be negligible for the pristine sample but were fit for the discharged samples.

NMR. NMR samples were stored under an inert atmosphere (dry N_2 gas), and the zirconia rotors were packed in an inert atmosphere glovebag (rotors had Teflon caps). The solid-phase material was ground to a powder in the inert atmosphere by mortar and pestle and loaded into the 2.5 mm rotors and capped. ^{51}V NMR data were acquired at a magnetic field strength of 13.9 T corresponding to a ^{51}V Larmor frequency of 155.1 MHz using a Tecmag Redstone spectrometer equipped with a Bruker 2.5 mm HX MAS probe. All ^{51}V MAS NMR spectra were obtained with a small tip angle (π/24) pulse acquire sequence under magic angle spinning (MAS) conditions ν_R = 10 kHz and 25 kHz with a 1 s recycle delay. A static ^{51}V NMR spectrum was obtained with a Hahn spin echo pulse sequence (τ = 40 μs).[29] Length of the 90-pulse was set at 0.7 μs and the recycle delay was 20 s. ^{51}V NMR spectra were referenced to a 0.1 M Na_3VO_4 solution (a secondary reference at −545 ppm relative to $VOCl_3$ at 0 ppm).[22] ^{51}V NMR data were simulated using the model "int2quad" within the Dmfit[30] program. All the discharged samples were similar in mass, typically 23−24 mg, and measurements were repeated twice.

The ^{31}P MAS NMR spectrum of pristine $Ag_2VO_2PO_4$ was acquired at 7 T with the corresponding Larmor frequency of 119.40 MHz (shown for reference in Supporting Information Figure S2). A Bloch decay pulse sequence was applied with 2.5 μs pulse widths (π/2 pulse), referenced to neat H_3PO_4, a 10 s recycle delay, recording 536 transients at 8 kHz MAS rotational frequency (ν_r).

For the ^{7}Li MAS NMR spectral data, samples were packed and unpacked under N_2. Spectra were acquired through Bloch decay with a small tip-angle pulse (1.5 μs) at a Larmor frequency of 116.47 MHz at 7 T. Samples were spun at 8 kHz with N_2 gas and recycle delays of 2s were used. The ^{7}Li MAS NMR spectral data for the 1ee, 2ee, and 3ee discharged SVPO samples can be found in Supporting Information Figures S3 and S4.

The error analysis of fitted experimental NMR parameters were performed by doing Monte Carlo simulations with Dmfit. The listed error values correspond to the 95% confidence interval of the fitted value (Supporting Information section S1 and Figure S5).

NMR Computational Methods. The package, CASTEP,[31] was used to perform density functional theory[32,33] (DFT) calculations of NMR parameters. Three SVPO structures from different sources were selected: a DFT-computed structure from the Materials Project,[34] a refined single-crystal SVPO structure by Lii and co-workers (ICSD-73580),[10] and a powder XRD SVPO structure Rietveld-refined by us. The DFT computations were performed using the generalized gradient approximations (GGA) and the Perdew−Burke−Ernzerhof[35−37] (PBE) functionals. The chemical shielding tensors[38,39] (or chemical shielding anisotropy, CSA) and electric field gradient (EFG)

https://doi.org/10.1021/acs.chemmater.1c00446
Chem. Mater. 2021, 33, 4425−4434

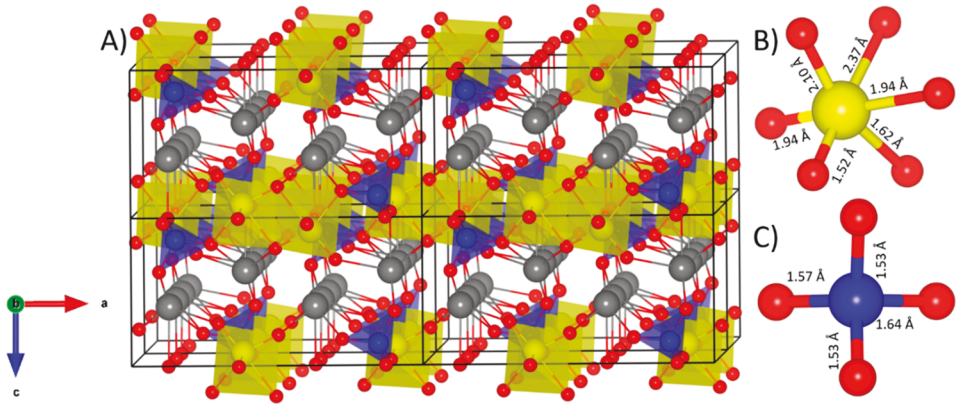

Figure 1. (A) Crystal structure of $Ag_2VO_2PO_4$, viewed down the *b*-axis. The vanadium octahedra (yellow) and the phosphorus tetrahedra (blue) form layers with silver (gray) interspersed in between. (B) Strongly distorted six-coordinate vanadium. (C) Slightly distorted phosphorus tetrahedra.

tensors[40] were calculated under the GIPAW[38,39] method utilizing ultrasoft pseudopotentials.[39] All the structures were geometry optimized first to the local minimum energy. The critical parameters (cutoff energy and k-point) used in the calculations were confirmed by convergence tests before the actual calculation to verify the calculation method (Supporting Information Figure S6).

Cell Construction. Type 2325 coin-type cells were assembled in an argon-filled glovebox. $Ag_2VO_2PO_4$ powder was pressed into pellets to construct cathodes. The anode was a disk of lithium metal and was separated from the cathode using polypropylene membranes wetted with $LiPF_6$ in 3:7 ethylene carbonate and dimethyl carbonate electrolyte.

Electrochemical Testing. Electrochemical impedance spectroscopy (EIS) of the assembled cells was collected with a Biologic VSP potentiostat/galvanostat, and fitting of the impedance was performed using ZView software (Supporting Information Figure S7 and Table S1). Discharge was performed at C/300 to 1ee, 2ee, and 3ee limits with a Maccor 4000 series battery-tester in a temperature-controlled chamber.

Ex Situ Testing. Electrodes were recovered from the coin-cells postdischarge by decrimping the cells under argon. The recovered $Ag_2VO_2PO_4$ pellet electrodes were rinsed with dimethyl carbonate and allowed to dry under argon before being packed and sealed under argon in Kapton tubes. The 28 ID-2 beamline at the National Synchrotron Light Source-II was calibrated to 0.2388 Å for collecting powder diffraction data. Measurements were collected by a CsI scintillator on an amorphous silicon detector. NIST standard LaB_6 powder was used to find instrumental broadening. GSAS-II[28] diffraction analysis software was used to refine the measured structure after integrating the 2D data as-collected to 1D data. The parameters refined were a background polynomial, scale parameters, atomic positions, Debye–Waller factors, and lattice parameters.

RESULTS AND DISCUSSION

The combination of X-ray diffraction and DSC analysis ascertains phase purity. DSC measured a single endothermic peak at 535 °C (Supporting Information Figure S8), which in previous reports supported by ICP-OES analysis has been attributed to $Ag_2VO_2PO_4$.[21,41,42] The structure of the synthesized material was confirmed by powder XRD. The diffraction pattern for pristine $Ag_2VO_2PO_4$ (SVPO) was found to match well with previous reports, PDF no. 01-081-2149 (calculated from FIZ no. 73580, March 18, 2008 by Jade, Supporting Information Figure S9), and a multiple unit cell graphical rendering of the structure is shown in Figure 1. Results of the powder diffraction including atomic coordinates and occupancies are shown in Supporting Information Table S2. The reported bond distances in the following paragraph are based on the results of the Rietveld refinement of powder diffraction.

$Ag_2VO_2PO_4$ forms a crystal in the *C*2/*m* space group as a layered structure. Pairs of six-coordinate vanadia species are associated edge-wise, and together with phosphate groups these form a full layer perpendicular to the (001) lattice direction. The six-coordinate vanadium sites are significantly distorted (see Figure 1) with vanadium–oxygen (V–O) bond distances between 1.52 and 2.37 Å. The phosphorus tetrahedra are only slightly distorted between 1.53 and 1.64 Å. Silver occupies the interlayer space, and the valence is estimated at +1. These ions coordinate with multiple oxygen atoms between 2.23 and 2.78 Å distances (Supporting Information Table S3). The crystal structure of the starting material permits the six-coordinate vanadium site(s) to be computed via DFT for interpretation by solid-state ^{51}V NMR. Because NMR is particularly sensitive to local electronic environments, any changes to this environment on discharge can be potentially interpreted even when the structure lacks the long-range order that is required for diffraction.

^{51}V SSNMR Spectroscopy of Pristine SVPO ($Ag_2VO_2PO_4$). ^{51}V NMR spectra were acquired at 13.9 T using static NMR and magic angle spinning (MAS) at multiple spinning frequencies (ν_R). Figure 2a and 2b (black) shows the experimental spectra of SVPO acquired at MAS rotational frequencies of 10 and 25 kHz, where symbols denote the isotropic resonances, centered at (δ_{iso} = −497 ppm). Accurate determination of the chemical shift anisotropy (CSA) tensor and the electric field gradient (EFG) tensor (Supporting Information eqs S1–S5) for ^{51}V in SVPO can be accomplished through experimental modeling (using a simulation package Dmfit) and calculation of the NMR tensors using a DFT package CASTEP.[31]

Using Dmfit to deconvolute the ^{51}V NMR spectra at two different MAS rotational frequencies, one can better assess the accuracy of the NMR parameters extracted. With simulation packages such as Dmfit, choosing the right model is critical to the success and accuracy of the simulation. ^{51}V has a small quadrupolar moment such that the width of the ^{51}V central transition is relatively narrow. Thus, the line shapes of ^{51}V NMR spectra are determined by a combination of both the CSA tensor and EFG tensor. We chose the "int2quad" model in Dmfit to perform the simulation because it takes into

https://doi.org/10.1021/acs.chemmater.1c00446
Chem. Mater. 2021, 33, 4425–4434

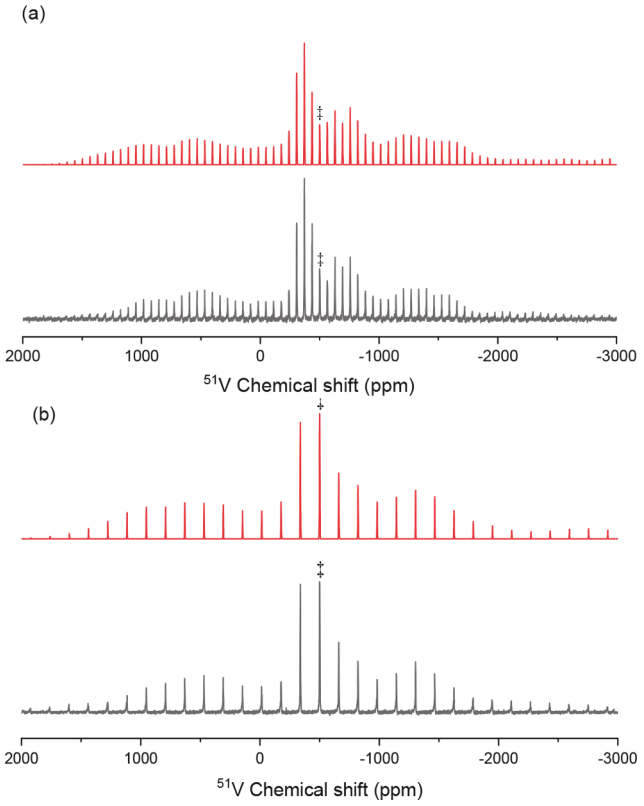

Figure 2. Experimental (black) and simulated (by Dmfit, red) using CASTEP-NMR tensor parameters as an "initial guess." ^{51}V MAS NMR spectra of $Ag_2VO_2PO_4$ obtained at 13.9T: (a) ν_R = 10 kHz and (b) ν_R = 25 kHz. Symbols (‡) indicate isotropic resonances.

account first- and second-order quadrupolar effects, and the effect of chemical shielding (shift) anisotropy. We use DFT calculated NMR parameters for the single vanadium site in SVPO as a "first guess" for Dmfit. Figure 2 shows the comparison between the experimental MAS NMR spectrum and the simulated spectrum from Dmfit. Excellent agreement is found between the simulated and experimental MAS NMR spectra, and the values from the deconvolution are shown in Table 1.

Calculation of NMR tensor values using DFT serves as an important part in the process of "NMR crystallography".[43,44] By comparing experimental NMR parameters with calculated NMR parameters (CSA and EFG tensors) based on structural models proposed by crystallographic methods such as XRD, validation or potentially further refinement of the atomic coordinates is possible. Here we perform DFT calculations of ^{51}V CSA and EFG tensors with three SVPO structural models with slightly different atomic coordinates from different sources (details are addressed in Experimental Section). The calculation results are summarized in Table 1.

Table 1 displays NMR tensors expressed in the Haeberlen convention, as well as values for chemical shift (δ, from experiment) and chemical shielding (σ, from computation) expressed in terms of the diagonalized tensor principal component values. Comparison between CASTEP shielding and experimental shift values requires referencing to a standard set of ^{51}V NMR compounds. Thus, the σ_{iso} and δ_{iso} values are not (directly) comparable between experiment and DFT computation. However, there is good agreement between the computed and experimental values of the other NMR parameters which are expressed in terms of the Haeberlen convention, such as the anisotropy of the chemical shift δ_{CS} (determined by the full diagonalized CSA tensor) and quadrupolar coupling constant C_Q (determined by the EFG tensor). The asymmetry parameter (η) of both CSA and EFG tensors (η_{CS} and η_Q), however, are not in as good agreement between experiment and theoretical calculations. This difficulty of accurately predicting asymmetry parameters is a familiar issue;[46] these expressions are more prone to error because the mathematical definition suffers from error propagation. The variation between CASTEP results for different structural models is small, which indicates good agreement of the structure with those published previously.

Even with such deviations, the static NMR spectrum can illustrate the subtle differences between models. To that end, a static ^{51}V NMR spectrum of pristine SVPO was recorded, shown in Figure 3. The experimental spectrum (black) is overlaid with the simulated static line shape (red) from Dmfit. The line shapes depicted represent both the central $\langle 1/2, -1/2 \rangle$ transition and multiple satellite transitions (for I = 7/2). The Dmfit-extracted NMR parameters are also shown in Table 1. The values obtained by fitting data for the static experiment agree well with those of the MAS results.

With the NMR parameters determined, local structure at the V sites can be further confirmed. The six-coordinate VO_6 species described here are edge-sharing dimers. Lapina et al.[22] report CSA anisotropy (δ_{cs}) in the range of −200 to −400 ppm

Table 1. Experimental and DFT ^{51}V NMR Parameters for $Ag_2VO_2PO_4$ (SVPO) by Haeberlen Convention Expressions[a]

pristine SVPO sample	δ_{iso} (ppm)	δ_{CS}	η_{CS}	C_Q (MHz)	η_Q
Experimental NMR Chemical Shift Anisotropy and Quadrupolar Parameters (fitted by Dmfit)					
SVPO (MAS at 10 kHz)	−497.2 ± 0.1	−416.0 ± 0.3	0.14 ± 0.03	5.53 ± 0.06	0.29 ± 0.01
SVPO (MAS at 25 kHz)	−496.5 ± 0.1	−413.4 ± 5.7	0.12 ± 0.03	5.47 ± 0.04	0.26 ± 0.01
SVPO (static NMR)	−495.2 ± 1.2	−416.6 ± 0.5	0.16 ± 0.001	5.47 ± 0.09	0.30 ± 0.01
	σ_{iso} (ppm)	δ_{CS}	η_{CS}	C_Q (MHz)	η_Q
DFT-Computed NMR Shielding and Quadrupolar Parameters[b]					
CASTEP SVPO#1 (computed)	−1530.4	−416.3	0.43	5.22	0.38
CASTEP SVPO#2 (single crystal XRD)	−1523.7	−413.7	0.42	5.23	0.35
CASTEP SVPO#3 (powder XRD)	−1518.7	−414.0	0.41	5.21	0.37

[a]Experimental measurements are expressed in terms of chemical shift (δ), and computed values are in terms of shielding (σ) (see Supporting Information Table S4 for individual tensor components). [b]CASTEP was used to calculate SVPO structures from three different sources: SVPO#1, computational structure from the Materials Project (MP-565532).[45] SVPO#2, a refined single-crystal SVPO structure by Lii and co-workers,[10] and SVPO#3, a powder diffraction SVPO structure Rietveld-refined by ourselves.

https://doi.org/10.1021/acs.chemmater.1c00446
Chem. Mater. 2021, 33, 4425−4434

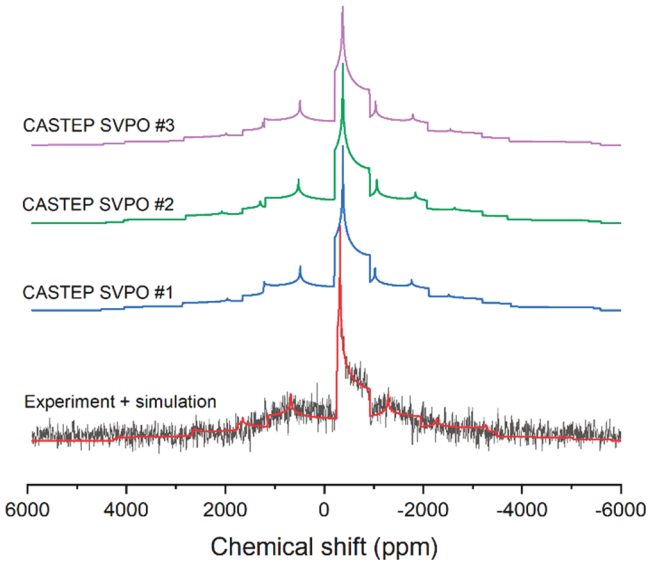

Figure 3. ^{51}V static SSNMR spectrum of $Ag_2VO_2PO_4$ obtained at 13.9T: experimental spectrum in black and Dmfit-simulated line shape in red. The central transition and all satellite transitions are all depicted in this spectrum. Overlaid are the multiple CASTEP-computed models from data in Table 1.

and CSA asymmetry parameters in the range of 0 to 0.2 for associated VO_6 species which are similar to our observations for SVPO. The isotropic chemical shifts found here for SVPO VO_6 edge-sharing dimers are in a range near to those reported for other VO_6 dimers (−500 to −560 ppm).[47,48]

Electrochemical Discharge. Coin cells assembled using a Li metal anode and $Ag_2VO_2PO_4$ cathode (Li||$Ag_2VO_2PO_4$) were discharged from their postassembly open circuit potential of about 3.40−3.55 V at a rate of C/300 (these discharge profiles are shown in Figure 4). Consistent with the high thermodynamic potential, yet low conductivity, of pristine SVPO, the initial potential rapidly drops to 2.3 V before recovering and leveling off at 2.6 V. The profiles observed are described by the following electrochemical processes:

$$Ag_2VO_2PO_4 + y\mathrm{Li} \rightarrow \mathrm{Li}_y\mathrm{Ag}_{2-y}VO_2PO_4 + y\mathrm{Ag}^0 \quad (1)$$

$$\mathrm{Li}_2VO_2PO_4 + z\mathrm{Li} \rightarrow \mathrm{Li}_{2+z}VO_2PO_4 \quad (2)$$

Initial reduction of SVPO involves the reduction of the Ag^+ ions, eq 1, and corresponds to the observed potential recovery from 2.3 to 2.6 V soon after discharge begins. As reduction proceeds, silver is displaced from the layered material as it aggregates to form a conductive Ag^0 matrix, and lithium ions intercalate in to balance charge. This reduction−displacement of silver from parent $Ag_2VO_2PO_4$ results in a drop in cell resistance and increase in conductivity. The second reaction, eq 2, represents the reduction of vanadium. These two electrochemical processes are not sequential, as it has been reported[49,50] that some V^{5+} is reduced to V^{4+} before Ag^0 formation ceases. The plateau region of the discharge profile up to 2.3 to 2.4 electron equivalents is dominated by Ag^0 formation while the downward sloping region after the plateau corresponds to reduction of V^{5+} to V^{4+}. Because the silver cations coordinate with a large number of oxygen atoms, formation of Ag^0 leads to the amorphization of the structure. Amorphization likely impedes further reduction−displacement of silver, which is a plausible explanation for the coreduction of silver and vanadium for a part of the discharge curve.[50] As discharge progresses, the magnetic susceptibility increases (although attenuation of magnetic susceptibilities for V^{3+} and V^{4+} in both vanadium oxides[51] and vanadium phosphates[52] is known, a measurable increase in the magnetic susceptibility of the discharged SVPO materials is clearly observed).[21] This increase cannot originate from an Ag center because the d^{10} electron configuration is maintained during Ag^+ reduction to Ag^0, neither of which display paramagnetic properties under these conditions.[53] Instead, the increase is assigned to the spin-moment calculations for both the d^1 and d^2 electron configurations, which result from two reduction events: $V^{5+} \rightarrow V^{4+} \rightarrow V^{3+}$. In addition, XAS spectra of $Ag_2VO_2PO_4$ at various points of discharge indicate that while Ag^+ is reduced, there is no formation of a single stable intermediate phase during the discharge; however, a binary Ag^0 and $Ag_2VO_2PO_4$ system is sufficient to fit the spectrum. Contributions from both the $Ag_2VO_2PO_4$ and Ag^0 phases to the discharged system absorption spectra, and an increase in magnetic susceptibility during the entirety of the discharge process, also support that V^{5+} and Ag^+ centers are reduced concurrently rather than sequentially.[21,50]

Bulk electrochemical reduction of pristine SVPO was conducted to generate 1ee, 2ee, and 3ee discharged samples. With each reduction step comes a loss of crystallinity, making

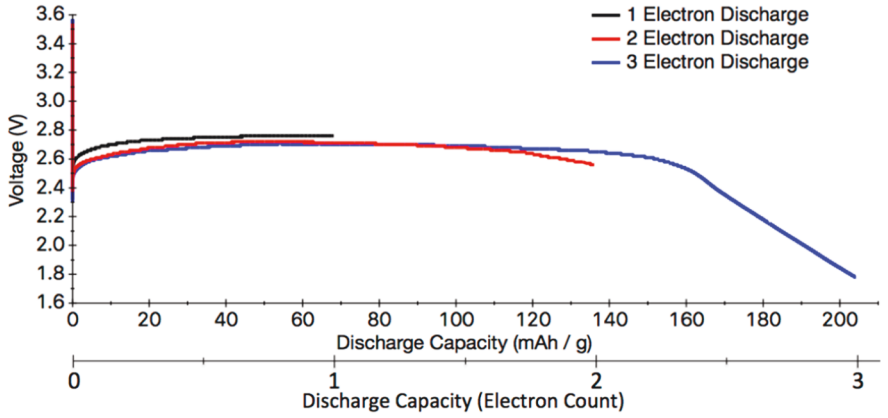

Figure 4. Discharge potential profiles at a rate of C/300 up to 1ee, 2ee, and 3ee discharged SVPO. The profile for the 2ee discharge profile is an average of multiple coin cells.

https://doi.org/10.1021/acs.chemmater.1c00446
Chem. Mater. 2021, 33, 4425−4434

these materials challenging to characterize. Compared to pristine SVPO, the 1ee reduced material is the most crystalline of the discharged samples, and a fitting analysis of the XRD data reveals that the material primarily consists of $Ag_2VO_2PO_4$ (~50%) and silver metal (~30%) along with small amounts of a (paramagnetic) lithiated vanadium phosphate phase (~10%) similar to $LiVOPO_4$ and some Li_2O (<10%) (Supporting Information Table S5). A crystallographic information file (CIF) of the refined 1ee discharged $Ag_2VO_2PO_4$ phase with strongly distorted VO_6 octahedral centers and slightly distorted PO_4 tetrahedral centers is provided in Supporting Information.

As previously mentioned, reduction leads to increased conductivity as Ag^0 deposits form and to an expansion of the interlayer distances as lithium ions intercalate between the layers of VO_6 and PO_4 polyhedra. The amorphization of the material upon reduction makes these materials challenging to characterize by XRD. XANES data have shown that the six-coordinate VO_6 environment is maintained throughout the discharge process despite severe distortion.[19] However, using detailed EXAFS analysis to determine local coordination environments is difficult due to beam attenuation by the electron-dense Ag atoms surrounding the V centers. Solid-state NMR is useful, as it can be used to monitor changes in the local site symmetry around vanadium upon reduction, including noncrystalline vanadium species that cannot be detected by XRD.

^{51}V SSNMR Spectroscopy of Discharged SVPO Samples. The atomic coordinates obtained from the Rietveld-refined structure of the $Ag_2VO_2PO_4$ component of the 1ee discharged sample depict the altered lattice for this first stage of electrochemical conversion (shown in Figure 5). The

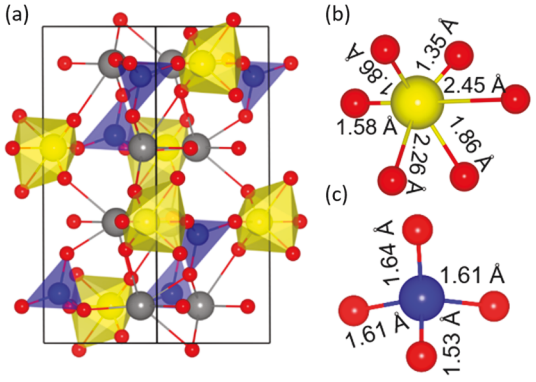

Figure 5. (a) Rietveld refined structure of 1ee discharged $Ag_2VO_2PO_4$ with VO_6 shown in yellow, PO_4 shown in blue and Ag atoms shown in gray. (b) Strongly distorted vanadium centers. (c) Slightly distorted phosphorus tetrahedra.

CASTEP-computed ^{51}V NMR EFG and chemical shielding tensors served as the starting point for Dmfit simulation of the ^{51}V MAS NMR spectrum (shown in red in Figure 6), which resolves a single vanadium site we assign to (1ee) $Ag_2VO_2PO_4$ (Table 2). When comparing ^{51}V NMR tensor values between those measured here to those of the SVPO parent compound (Table 1), it is notable that the isotropic resonance remains essentially the same. Observation of a single isotropic resonance suggests that the ^{51}V species that are observed are in a homogeneous environment and not distributed among different structural domains. The XRD data indicate that while the major component of the 1ee discharged SVPO sample is

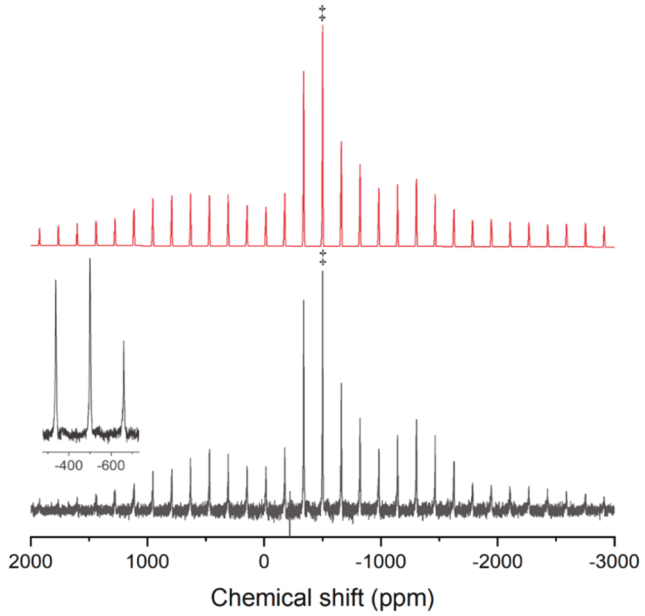

Figure 6. ^{51}V MAS NMR of 1ee discharged $Ag_2VO_2PO_4$, obtained at 13.9 T and ν_R = 25 kHz MAS. Experimental (black) and simulated (by Dmfit the "int2quad" model, red) using CASTEP-NMR tensor parameters as an "initial guess". Symbols (‡) indicate isotropic resonances. Inset image shows expansion of the region near the isotropic resonance.

$Ag_2VO_2PO_4$, there are local changes about the VO_6 and PO_4 centers. Significant changes to the crystal structure can be seen through comparison of pristine SVPO (Figure 1) to that of the 1ee discharged sample (Figure 5). Figures S10 and S11 in Supporting Information graphically depict changes to the V−O bond lengths to illustrate the shift of atoms that occurs in a pair of edge-sharing VO_6 centers upon reduction. These changes in the local structure are reflected in a significant change in the ^{51}V NMR chemical shift anisotropy (δ_{CS}) and a measurable difference in the quadrupolar coupling constant (C_Q). In a study of a series of $Li_xV_2O_5$ ($0.4 < x < 1.4$) materials, Nakamura et al.[54] also found that as V^{5+} is reduced, the ^{51}V NMR isotropic chemical shift stays approximately the same while δ_{CS} and C_Q change. It is worth noting that for both the $Li_xV_2O_5$ study and this study, the ^{51}V NMR tensor parameters (δ_{CS} and C_Q) better reflect changes to the local environment than the isotropic chemical shift.

The further reduced samples were also analyzed by ^{51}V NMR spectroscopy, and solid-state MAS spectra for the 2ee and 3ee reduced samples (along with the 1ee reduced sample) are shown in Figure 7. For the 1ee discharged material, the majority of the vanadium is still diamagnetic V^{5+}. As reduction proceeds, a substantial loss of signal intensity is observed. These findings are consistent with a paramagnetic sample, as expected for V^{4+} ($Li_{2+z}VO_2PO_4$). The reduction of diamagnetic V^{5+} to a lower 4+ oxidation state leads to paramagnetic vanadium species and a concomitant increase in magnetic susceptibility.[21] The strong unpaired electron−nuclear interaction leads to a very fast T_2 relaxation which makes paramagnetic V^{4+} and V^{3+} undetectable by NMR.[55] As expected, this increase in paramagnetic character leads to a decrease in signal/noise (S/N) ratio due to the lower abundance of detectable V^{5+}. According to the electrochemical discharge data, Ag^+ is initially reduced to Ag^0. However, Ag^+ is

https://doi.org/10.1021/acs.chemmater.1c00446
Chem. Mater. 2021, 33, 4425−4434

Table 2. Experimental ^{51}V NMR Chemical Shift Anisotropy and Quadrupolar Parameters (fitted by Dmfit) for Electrochemically Discharged SVPO Structures by Haeberlen Convention Expressions[a]

discharged SVPO sample	δ_{iso} (ppm)	δ_{CS}	η_{CS}	C_Q (MHz)	η_Q
1ee discharged (MAS at 25 kHz)	−496.0 ± 0.1	−380.6 ± 6.3	0.21 ± 0.05	5.30 ± 0.02	0.26 ± 0.01
2ee discharged (MAS at 25 kHz)	−496.0 ± 0.1	−383.0 ± 11.0	0.18 ± 0.13	5.20 ± 0.06	0.25 ± 0.02
3ee discharged (MAS at 25 kHz)	−496.0 ± 0.2	–	–	–	–

[a]Experimental measurements are expressed in terms of chemical shift (δ) (see Supporting Information Table S4 for individual tensor components).

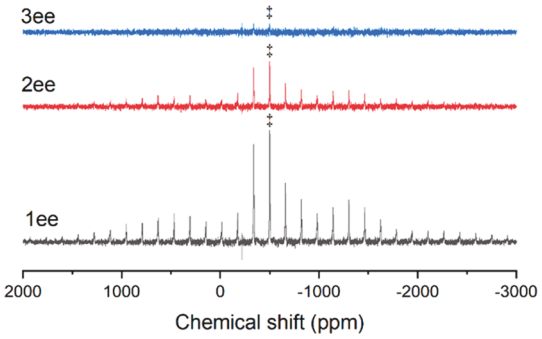

Figure 7. Comparison of the ^{51}V MAS NMR spectra of 1ee, 2ee, and 3ee discharged $Ag_2VO_2PO_4$, obtained at 13.9 T and ν_R = 25 kHz MAS. The same number of scans were collected for each spectrum. Symbols (‡) indicate isotropic resonances.

not completely reduced prior to reduction of V^{5+}; these occur concurrently.[50] The magnetic susceptibility of the material increases with each reduction step, although not in a linear fashion; on the basis of these NMR data, the 1ee discharged SVPO sample only contains a small amount of paramagnetic material, whereas the 3ee discharged SVPO sample contains the largest amount.[21] Notably, the magnetic susceptibility of the 2ee discharged material more closely resembles that of the 3ee discharged material. The isotropic chemical shift values for both the pristine SVPO and the discharged SVPO compounds do not change, indicating that the ^{51}V NMR spectrum of V^{5+} receives limited influence from paramagnetic V^{4+} and V^{3+}. The increased paramagnetic behavior along with the increase in uncertainty of the XRD structural model with the onset of reduction introduces complications in the CASTEP calculations of the 1ee sample, rendering the modeling of the tensors to be uncertain.

The ^{51}V MAS NMR spectrum of the 2ee discharged $Ag_2VO_2PO_4$ is shown in greater detail in Figure 8. We were able to use Dmfit to deconvolute the spectrum of the 2ee discharged sample. Although the XRD analysis of the 2ee discharged sample of $Ag_2VO_2PO_4$ was performed, the amorphization of SVPO upon reduction along with the presence of multiple components severely complicates any type of detailed structure analysis through diffraction methods. In fact, the XRD analysis indicates that the crystalline portion of the 2ee discharged sample consists primarily of silver metal (over 80%) along with small amounts of starting $Ag_2VO_2PO_4$ (~10%) and approximately 10% of a lithiated vanadium phosphate phase ($LiVOPO_4$) (Supporting Information Table S5). While refined phase fractions of the phases identified in the 2ee discharged $Ag_2VO_2PO_4$ identified all significant diffraction features, they did not account for all vanadium and oxygen atoms present based on material stoichiometry. It was therefore assumed that the remaining moles of vanadium and oxygen belonged to an amorphous $Li_xVO_yPO_4$ phase (Table S5). In the absence of a crystallographic model

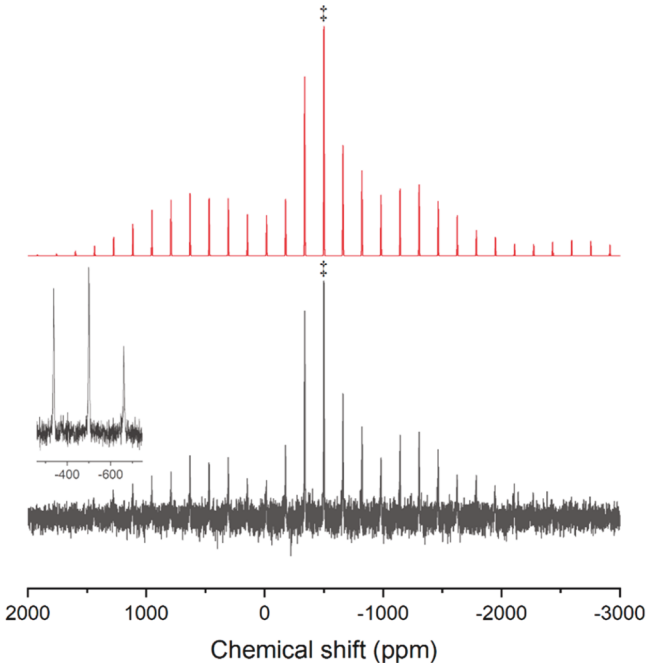

Figure 8. ^{51}V MAS NMR of 2ee discharged $Ag_2VO_2PO_4$, obtained at 13.9 T and ν_R = 25 kHz MAS. Experimental (black) and simulated by Dmfit the "int2quad" model (red) using the 1ee discharged spectrum. Symbols (‡) indicate isotropic resonances.

structure, we were not able to use CASTEP to calculate the NMR spectral data for the 2ee and 3ee discharged material with desired accuracy.

What is lacking from the XRD analysis is any information about the amorphous material that is present. Analyzing the 2ee discharged sample using ^{51}V SSNMR reveals that the isotropic resonance remains the same as the pristine and the 1ee discharged SVPO. Therefore, the ^{51}V NMR spectrum of the 2ee discharged SVPO sample provides a (narrow) window into this material, suggestive of regions of the sample that retain some unreacted V^{5+}. Unfortunately, because we do not detect any other paramagnetic phases, we are unable to make further conclusions about the mechanism of this reduction process.

This study, connecting XRD structure to NMR parameters (extracted from experimental data), is a first step along the pathway toward predicting distortions to the VO_6 sites. The general trend from pristine to 1ee to 2ee discharged SVPO is that the anisotropy of the CSA (δ_{CS}) changes with increasing discharge, from −416 ppm in pristine SVPO to approximately −380 ppm in the reduced samples, and the C_Q decreases slightly in magnitude (from 5.5 MHz in pristine SVPO to 5.2 MHz in the 2ee discharged sample). Although we may be observing only a fraction of the structure (i.e., that which is diamagnetic) in these more reduced samples, the data provide NMR tensors that are indicative of the electronic environment

https://doi.org/10.1021/acs.chemmater.1c00446
Chem. Mater. 2021, 33, 4425−4434

at the V^{5+} sites, showing that distortion of the diamagnetic VO_6 centers continues before further reduction causes a loss of signal.

It is important to note that a NMR spectral study of the commercially important silver vanadium oxide ($Ag_2V_4O_{11}$, SVO) was reported in 2007 by Greenbaum and co-workers.[20] The NMR analysis focused on the ^{7}Li SSNMR data of reduced SVO (~1ee up to ~6ee discharged SVO) which showed evidence of Li^+ ions in three different environments corresponding to three separate voltage plateaus. Here we provide representative ^{7}Li NMR spectral data of the discharged SVPO samples (Supporting Information Figures S3 and S4) without a detailed analysis. Although there are similarities between the ^{7}Li NMR data of SVPO and SVO (evidence of Li^+ in different environments and broadening of peaks with increased discharge), we focused our attention on the ^{51}V nucleus which is a more sensitive probe in elucidating structural changes within this material. Leifer et al. did report the ^{51}V NMR data (quadrupolar echo) of pristine SVO as well as some of that of the reduced samples.[20] Like the changes we observed for the 1ee reduction of SVPO, they observed minor changes in the central transition as well as the quadrupolar satellite transitions in the ^{51}V NMR spectral data of $Li_{0.72}Ag_2V_4O_{11}$ (~1ee discharged SVO) with pristine SVO. Thus, the crystallinity and local environment about vanadium are not substantially altered during the early stages of reduction for SVO as well as SVPO. The spectral data for the ~2ee discharged SVO sample visually displays noticeable differences when compared with the data of pristine SVO, and further reduction (~6ee discharged SVO) leads to a significant loss of signal which is expected as the paramagnetic properties of the sample increase as V^{5+} is reduced. The chemical shielding (shift) values are useful to researchers when trying to understand the components present in an amorphous material, and here we are reporting several sites that may be useful to test structural models of the discharged, amorphous SVPO. Instead of visually comparing the line shapes, utilizing Dmfit and CASTEP to extract NMR line shape parameters has enabled us to conduct an analysis that reflects the vanadium local environment, and we find similar observations between the two systems.

CONCLUSIONS

Spectroscopic analysis of SVPO and related discharged materials has been conducted. Dmfit was utilized to determine key NMR parameters for pristine and 1ee and 2ee discharged SVPO. CASTEP DFT calculations were also applied to pristine SVPO samples. Good agreement was found between the DFT and experimental parameters for pristine SVPO material. The data reveal that while the isotropic chemical shift does not change substantially upon reduction of the material, there are significant changes in the reduced chemical shift anisotropy and the quadrupolar coupling constant. These changes, manifested as NMR line shape differences, indicate that while the local coordination environment of VO_6 dimers is maintained throughout the reduction process, there are deviations in the local symmetry about the VO_6 center. This is information that could not be obtained from XRD data because there is a significant loss of crystallinity in the vanadium phases after more than 1ee have been added. Therefore, the sensitivity of SSNMR to local coordination environments provides a rare window into the structure, when it lacks long-range order, of the amorphous, reduced samples. Possession of NMR tensors such as these could one day enable modeling of amorphous vanadium oxide structures containing V^{5+}.

ASSOCIATED CONTENT

Supporting Information

The Supporting Information is available free of charge at https://pubs.acs.org/doi/10.1021/acs.chemmater.1c00446.

^{31}P and ^{7}Li NMR, DSC, EIS, XRD, Rietveld refinement parameters and bond lengths, DFT convergence tests, NMR tensors and equations, statistical analysis of experimental NMR parameters with Monte Carlo simulations, principal components of experimental and DFT calculated NMR shift/shielding tensors for pristine $Ag_2VO_2PO_4$, refined weight fractions at different levels of discharge, and visualization of the V_2O_{10} units from XRD (PDF)

CIF file for the 1ee discharged $Ag_2VO_2PO_4$ phase (CIF)

AUTHOR INFORMATION

Corresponding Authors

Amy C. Marschilok − *Department of Chemistry, Institute for Electrochemically Stored Energy, and Department of Materials Science and Chemical Engineering, Stony Brook University, Stony Brook, New York 11794, United States; Interdisciplinary Science Department, Brookhaven National Laboratory, Upton, New York 11973, United States;* orcid.org/0000-0001-9174-0474; Email: amy.marschilok@stonybrook.edu

Sophia E. Hayes − *Department of Chemistry, Washington University in St. Louis, St. Louis, Missouri 63130-4899, United States;* orcid.org/0000-0002-2809-6193; Email: hayes@wustl.edu

Lisa F. Szczepura − *Department of Chemistry, Illinois State University, Normal, Illinois 61790-4160, United States;* orcid.org/0000-0002-1464-1285; Email: lfszcze@IllinoisState.edu

Authors

He Sun − *Department of Chemistry, Washington University in St. Louis, St. Louis, Missouri 63130-4899, United States;* orcid.org/0000-0002-1887-1643

Blake A. Hammann − *Department of Chemistry, Washington University in St. Louis, St. Louis, Missouri 63130-4899, United States*

Alexander B. Brady − *Department of Materials Science and Chemical Engineering, Stony Brook University, Stony Brook, New York 11794, United States*

Gurpreet Singh − *Department of Chemistry and Institute for Electrochemically Stored Energy, Stony Brook University, Stony Brook, New York 11794, United States*

Lisa M. Housel − *Institute for Electrochemically Stored Energy, Stony Brook University, Stony Brook, New York 11794, United States; Interdisciplinary Science Department, Brookhaven National Laboratory, Upton, New York 11973, United States;* orcid.org/0000-0001-8429-5480

Esther S. Takeuchi − *Department of Chemistry, Institute for Electrochemically Stored Energy, and Department of Materials Science and Chemical Engineering, Stony Brook University, Stony Brook, New York 11794, United States; Interdisciplinary Science Department, Brookhaven National*

Laboratory, Upton, New York 11973, United States; orcid.org/0000-0001-8518-1047

Kenneth J. Takeuchi − *Department of Chemistry, Institute for Electrochemically Stored Energy, and Department of Materials Science and Chemical Engineering, Stony Brook University, Stony Brook, New York 11794, United States; Interdisciplinary Science Department, Brookhaven National Laboratory, Upton, New York 11973, United States;* orcid.org/0000-0001-8129-444X

Complete contact information is available at: https://pubs.acs.org/10.1021/acs.chemmater.1c00446

Notes

The authors declare no competing financial interest.

■ ACKNOWLEDGMENTS

This material is based on work supported by the National Science Foundation (NSF CHE RUI 1401686 to L.F.S.). This work is also supported (for H.S. and S.E.H.) by the National Science Foundation (NSF OAC 1640899). This work made use of computational resources and software infrastructure provided by the Washington University Center for High-Performance Computing (CHPC) at the Mallinckrodt Institute for Radiology. The authors thank Katie Wentz and Robert Marti for collecting some of the initial spectral data. The materials synthesis, materials characterization via XRD and DSC, preparation of the electrochemical cells, and electrochemical analysis were supported as part of the Center for Mesoscale Transport Properties, an Energy Frontier Research Center supported by the U.S. Department of Energy, Office of Science, Basic Energy Sciences, under award no. DE-SC0012673. E.S.T. acknowledges the William and Jane Knapp Chair in Energy and the Environment.

■ REFERENCES

(1) Takeuchi, K. J.; Marschilok, A. C.; Davis, S. M.; Leising, R. A.; Takeuchi, E. S. Silver vanadium oxides and related battery applications. *Coord. Chem. Rev.* **2001**, *219*−*221*, 283−310.

(2) Tracey, A. S.; Willsky, G. R.; Eds. Vanadium: Chemistry, Biochemistry Pharmacology and Practical Applications; CRC Press: Boca Raton, FL, 2007; Chapter 13.

(3) Hu, J.; Huang, W.; Yang, L.; Pan, F. Structure and performance of the $LiFePO_4$ cathode material: from the bulk to the surface. *Nanoscale* **2020**, *12*, 15036−15044.

(4) Yang, D.; Dai, Y.; Wang, S.; Yu, J. How to make lithium iron phosphate better: a review exploring classical modification approaches in-depth and proposing future optimization methods. *J. Mater. Chem. A* **2016**, *4*, 18210−18222.

(5) Padhi, A. K.; Nanjundaswamy, K. S.; Goodenough, J. B. Phospho-olivines as Positive-Electrode Materials for Rechargeable Lithium Batteries. *J. Electrochem. Soc.* **1997**, *144*, 1188−1194.

(6) Zhang, W.-J. Structure and performance of $LiFePO_4$ cathode materials: A review. *J. Power Sources* **2011**, *196*, 2962−2970.

(7) Chung, S.-Y.; Bloking, J. T.; Chiang, Y.-M. Electronically conductive phospho-olivines as lithium storage electrodes. *Nat. Mater.* **2002**, *1*, 123−128.

(8) Yu, F.; Zhang, L.; Li, Y.; An, Y.; Zhu, M.; Dai, B. Mechanism studies of $LiFePO_4$ cathode material: lithiation/delithiation process, electrochemical modification and synthetic reaction. *RSC Adv.* **2014**, *4*, 54576−54602.

(9) Zaghib, K.; Charest, P.; Guerfi, A.; Shim, J.; Perrier, M.; Striebel, K. Safe Li-ion polymer batteries for HEV applications. *J. Power Sources* **2004**, *134*, 124−129.

(10) Kang, H.-Y.; Wang, S.-L.; Tsai, P.-P.; Lii, K.-W. Hydrothermal Synthesis, Crystal Structure and Ionic Conductivity of $Ag_2VO_2PO_4$: a New Layered Phosphate of Vanadium(V). *J. Chem. Soc., Dalton Trans.* **1993**, 1525.

(11) Stenina, I. A.; Yaroslavtsev, A. B. Nanomaterials for lithium-ion batteries and hydrogen energy. *Pure Appl. Chem.* **2017**, *89*, 1185−1194.

(12) Yi, T.-F.; Li, X.-Y.; Liu, H.; Shu, J.; Zhu, Y.-R.; Zhu, R.-S. Recent developments in the doping and suface modification of $LiFePO_4$ as cathode material for power lithium ion battery. *Ionics* **2012**, *18*, 529−539.

(13) Jiang, W.; Wu, M.; Liu, F.; Yang, J.; Feng, T. Variation of carbon coatings on the electrochemical performance of $LiFePO_4$ cathodes for lithium ionic Batteries. *RSC Adv.* **2017**, *7*, 44296−44302.

(14) Gao, L.; Xu, Z.; Zhang, S.; Xu, J.; Tang, K. Enhanced electrochemical properties of $LiFePO_4$ cathode materials by Co and Zr multi-doping. *Solid State Ionics* **2017**, *305*, 52−56.

(15) Anguchamy, Y.-K.; Lee, J.-W.; Popov, B. N. Electrochemical performance of polypyrrole/silver vanadium oxide composite cathodes in lithium primary batteries. *J. Power Sources* **2008**, *184*, 297−302.

(16) Leising, R. A.; Gleason, N. R.; Palazzo, M.; Takeuchi, E. S.; Takeuchi, K. J. Presented at *208th Meeting of the Electrochemical Society. Session D2− Rechargeable Lithium and Lithium-ion Batteries − Battery/Energy Technology*, Los Angeles, CA, Oct 16−21, 2005.

(17) Morcrette, M.; Martin, P.; Rozier, P.; Vezin, H.; Chevallier, F.; Laffont, L.; Poizot, P.; Tarascon, J.-M. $Cu_{1.1}V_4O_{11}$: A New Positive Electrode Material for Rechargeable Li Batteries. *Chem. Mater.* **2005**, *17*, 418−426.

(18) Morcrette, M.; Rozier, P.; Dupont, L.; Mugnier, E.; Sannier, L.; Galy, J.; Tarascon, J.-M. A reversible copper extrusion−insertion electrode for rechargeable Li batteries. *Nat. Mater.* **2003**, *2*, 755−761.

(19) Takeuchi, E. S.; Marschilok, A. C.; Tanzil, K.; Kozarsky, E. S.; Zhu, S.; Takeuchi, K. J. Electrochemical Reduction of Silver Vanadium Phosphorus Oxide, $Ag_2VO_2PO_4$: The Formation of Electrically Conductive Metallic Silver Nanoparticles. *Chem. Mater.* **2009**, *21*, 4934−4939.

(20) Leifer, N. D.; Colon, A.; Martocci, K.; Greenbaum, S. G.; Alamgir, F. M.; Reddy, T. B.; Gleason, N. R.; Leising, R. A.; Takeuchi, E. S. Nuclear Magnetic Resonance and X-Ray Absorption Spectroscopic Studies of Lithium Insertion in Silver Vanadium Oxide Cathodes. *J. Electrochem. Soc.* **2007**, *154*, A500−A506.

(21) Marschilok, A. C.; Kozarsky, E. S.; Tanzil, K.; Zhu, S.; Takeuchi, K. J.; Takeuchi, E. S. Electrochemical reduction of silver vanadium phosphorous oxide, $Ag_2VO_2PO_4$: Silver metal deposition and associated increase in electrical conductivity. *J. Power Sources* **2010**, *195*, 6839−6846.

(22) Lapina, O. B.; Khabibulin, D. F.; Shubin, A. A.; Terskikh, V. V. Practical aspects of ^{51}V and ^{93}Nb solid-state NMR spectroscopy and applications to oxide materials. *Prog. Nucl. Magn. Reson. Spectrosc.* **2008**, *53*, 128−191.

(23) Rehder, D.; Polenova, T.; Bühl, M. Vanadium-51 NMR. *Annu. Rep. NMR Spectrosc.* **2007**, *62*, 49−114.

(24) Rehder, D. The (biological) speciation of vanadate(V) as revealed by ^{51}V NMR: A tribute on Lage Pettersson and his work. *J. Inorg. Biochem.* **2015**, *147*, 25−31.

(25) Schwendt, P.; Tatiersky, J.; Krivosudsky, L.; Simunekova, M. Peroxido complexes of vanadium. *Coord. Chem. Rev.* **2016**, *318*, 135−157.

(26) Pooransingh-Margolis, N.; Renirie, R.; Hasan, Z.; Wever, R.; Vega, A. J.; Polenova, T. ^{51}V Solid-State Magic Angle Spinning NMR Spectroscopy of Vanadium Chloroperoxidase. *J. Am. Chem. Soc.* **2006**, *128*, 5190−5208.

(27) Lapina, O. B.; Shubin, A. A.; Khabibulin, D. F.; Terskikh, V. V.; Bodart, P. R.; Amoureux, J.-P. Solid-state ^{51}V NMR for characterization of vanadium- containing systems. *Catal. Today* **2003**, *78*, 91−104.

(28) Toby, B. H.; Von Dreele, R. B. GSAS-II: the genesis of a modern open-source all purpose crystallography software package. *J. Appl. Crystallogr.* **2013**, *46*, 544−549.

(29) Kunwar, A. C.; Turner, G. L.; Oldfield, E. Solid-State Spin-Echo Fourier Transform NMR of ^{39}K and ^{67}Zn Salts at High Field. *J. Magn. Reson.* **1986**, *69*, 124−127.
(30) Massiot, D.; Fayon, F.; Capron, M.; King, I.; Le Calvé, S.; Alonso, B.; Durand, J.-O.; Bujoli, B.; Gan, Z.; Hoatson, G. Modelling one- and two- dimensional solid-state NMR spectra. *Magn. Reson. Chem.* **2002**, *40*, 70−76.
(31) Clark, S. J.; Segall, M. D.; Pickard, C. J.; Hasnip, P. J.; Probert, M. I. J.; Refson, K.; Payne, M. C. First principles methods using CASTEP. *Z. Kristallogr. - Cryst. Mater.* **2005**, *220*, 567−570.
(32) Hohenberg, P.; Kohn, W. Inhomogeneous Electron Gas. *Phys. Rev.* **1964**, *136*, B864−B871.
(33) Kohn, W.; Sham, L. J. Self-consistent equations including exchange and correlation effects. *Phys. Rev.* **1965**, *140*, A1133−A1138.
(34) Jain, A.; Ong, S. P.; Hautier, G.; Chen, W.; Richards, W. D.; Dacek, S.; Cholia, S.; Gunter, D.; Skinner, D.; Ceder, G.; Persson, K. A. The Materials Project: A materials genome approach to accelerating materials innovation. *APL Mater.* **2013**, *1*, 011002.
(35) Perdew, J. P.; Burke, K.; Ernzerhof, M. Generalized Gradient Approximation Made Simple. *Phys. Rev. Lett.* **1996**, *77*, 3865−3868.
(36) Perdew, J. P.; Burke, K.; Ernzerhof, M. Perdew, Burke, and Ernzerhof Reply: *Phys. Rev. Lett.* **1998**, *80*, 891.
(37) Hammer, B.; Hansen, L. B.; Nørskov, J. K. Improved adsorption energetics within density-functional theory using revised Perdew-Burke-Ernzerhof functionals. *Phys. Rev. B: Condens. Matter Mater. Phys.* **1999**, *59*, 7413−7421.
(38) Pickard, C. J.; Mauri, F. All-electron magnetic response with pseudopotentials: NMR chemical shifts. *Phys. Rev. B: Condens. Matter Mater. Phys.* **2001**, *63*, 245101.
(39) Yates, J. R.; Pickard, C. J.; Mauri, F. Calculation of NMR chemical shifts for extended systems using ultrasoft pseudopotentials. *Phys. Rev. B: Condens. Matter Mater. Phys.* **2007**, *76* (1−11), 024401.
(40) Ferrage, F.; Zoonens, M.; Warschawski, D. E.; Popot, J.-L.; Bodenhausen, G. Slow Diffusion of Macromolecular Assemblies by a New Pulsed Field Gradient NMR Method. *J. Am. Chem. Soc.* **2003**, *125*, 2541−2548.
(41) Bock, D. C.; Marschilok, A. C.; Takeuchi, K. J.; Takeuchi, E. S. A kinetics and equilibrium study of vanadium dissolution from vanadium oxides and phosphates in battery electrolytes: Possible impacts on ICD battery performance. *J. Power Sources* **2013**, *231*, 219−225.
(42) Huang, J.; Marschilok, A. C.; Takeuchi, E. S.; Takeuchi, K. J. Microwave-assisted synthesis of silver vanadium phosphorus oxide, $Ag_2VO_2PO_4$: crystallite size control and impact on electrochemistry. *Chem. Mater.* **2016**, *28*, 2191−2199.
(43) Ashbrook, S. E.; McKay, D. Combining solid-state NMR spectroscopy with first-principles calculations − a guide to NMR crystallography. *Chem. Commun.* **2016**, *52*, 7186−7204.
(44) Martineau, C.; Senker, J.; Taulelle, F. Chapter One − NMR Crystallography. *Annu. Rep. NMR Spectrosc.* **2014**, *82*, 1−57.
(45) de Jong, M.; Chen, W.; Angsten, T.; Jain, A.; Notestine, R.; Gamst, A.; Sluiter, M.; Krishna Ande, C.; van der Zwaag, S.; Plata, J. J.; Toher, C.; Curtarolo, S.; Ceder, G.; Persson, K. A.; Asta, M. Charting the complete elastic properties of inorganic crystalline compounds. *Sci. Data* **2015**, *2*, 150009.
(46) Sun, H.; Dwaraknath, S.; Ling, H.; Qu, X.; Huck, P.; Persson, K. A.; Hayes, S. E. Enabling materials informatics for ^{29}Si solid-state NMR of crystalline materials. *npj Computational Materials* **2020**, *6*, 53.
(47) Huang, W.; Todaro, L.; Francesconi, L. C.; Polenova, T. ^{51}V Magic Angle Spinning NMR Spectroscopy of Six-Coordinate Lindqvist Oxoanions: A Sensitive Probe for the Electronic Environment in Vanadium-Containing Polyoxometalates. Counterions Dictate the ^{51}V Fine Structure Constants in Polyoxometalate Solids. *J. Am. Chem. Soc.* **2003**, *125*, 5928.
(48) Huang, W.; Todaro, L.; Yap, G. P. A.; Beer, R.; Francesconi, L. C.; Polenova, T. ^{51}V Magic Angle Spinning NMR Spectroscopy of Keggin Anions $[PV_nW_{12-n}O_{40}]^{(3+n)-}$: Effect of Countercation and Vanadium Substitution on Fine Structure Constants. *J. Am. Chem. Soc.* **2004**, *126*, 11564−11573.
(49) Partridge, C. J.; Jaye, C.; Abtew, T. A.; Ravel, B.; Fischer, D. A.; Marschilok, A. C.; Zhang, P.; Takeuchi, K. J.; Takeuchi, E. S.; Banerjee, S. An X-ray Absorption Spectroscopy Study of the Cathodic Discharge of $Ag_2VO_2PO_4$: Geometric and Electronic Structure Characterization of Intermediate phases and Mechanistic Insights. *J. Phys. Chem. C* **2011**, *115*, 14437−14447.
(50) Zhang, R.; Abtew, T. A.; Quackenbush, N. F.; Wangoh, L. W.; Huie, M.; Brady, A. B.; Bock, D.; Efstathiadis, H.; Whittingham, M. S.; Marschilok, A. C.; Takeuchi, K. J.; Takeuchi, E. S.; Zhang, P.; Piper, L. F. J. Electrode Reaction Mechanism of $Ag_2VO_2PO_4$ Cathode. *Chem. Mater.* **2016**, *28*, 3428−3434.
(51) Chamberland, B. L.; Porter, S. K. A study on the preparation and physical property determination of $NaVO_2$. *J. Solid State Chem.* **1988**, *73*, 398−404.
(52) Nath, R.; Tsirlin, A. A.; Rosner, H.; Geibel, C. Magnetic properties of $BaCdVO(PO_4)_2$: A strongly frustrated spin-1 2 square lattice close to the quantum critical regime. *Phys. Rev. B: Condens. Matter Mater. Phys.* **2008**, *78* (6), 064422.
(53) Dupree, R.; Ford, C. J. Magnetic Moments of the Noble Metals around their melting points. *Phys. Rev. B* **1973**, *8*, 1780−1782.
(54) Nakamura, K.; Nishioka, D.; Michihiro, Y.; Vijayakumar, M.; Selvasekarapandian, S.; Kanashiro, T. ^{7}Li and ^{51}V NMR study on Li^+ ionic diffusion in lithium intercalated $Li_xV_2O_5$. *Solid State Ionics* **2006**, *177*, 129−135.
(55) Ooms, K.; Polenova, T.; Shough, A.-M.; Doren, D. J.; Nash, M. J.; Lobo, R. F. Identification of Mixed Valence Vanadium in ETS-10 Using Electron Paramagnetic Resonance, ^{51}V Solid-State Nuclear Magnetic Resonance, and Density Functional Theory Studies. *J. Phys. Chem. C* **2009**, *113*, 10477−10484.

https://doi.org/10.1021/acs.chemmater.1c00446
Chem. Mater. 2021, 33, 4425−4434